Full Length Article

Fluid dynamics of oscillatory flow across parallel-plates in standing-wave thermoacoustic system with two different operation frequencies

Waleed Almukhtar Allafi [a], Fatimah Al Zahrah Mohd Saat [a,b,*], Xiaoan Mao [c]

[a] Fakulti Kejuruteraan Mekanikal, Universiti Teknikal Malaysia Melaka, Hang Tuah Jaya, 76100 Durian Tunggal, Melaka, Malaysia
[b] Centre for Advanced Research on Energy, Universiti Teknikal Malaysia Melaka, hang Tuah Jaya, 76100 Durian Tunggal, Melaka, Malaysia
[c] Faculty of Engineering and Physical Sciences, University of Leeds, Leeds, United Kingdom

ARTICLE INFO

ABSTRACT

Thermoacoustic system is one of the alternative technologies that provides green working principles but the lack of understanding of the complex fluid flow and energy transfer interactions within structures inside the system is leading to difficulty in accurate analysis related to the system. This study presents fluid dynamic investigation of vortex shedding and velocity profile of an oscillatory flow across a parallel-plate structure inside a standing-wave thermoacoustic system by using a two-dimensional ANSYS FLUENT CFD (computational fluid dynamics) of SST k-ω turbulence model. The model was validated using experimental data and theoretical solution. Two different operating frequencies of 14.2 Hz and 23.6 Hz were investigated with drive ratios (defined as maximum pressure amplitude to mean pressure) from 0.3% up to 3%. The results revealed that velocity profiles and boundary layers within the area of parallel-plate stack changes with time and the changes followed the cyclic travel of vortex across the structure. Two layers of vortex formed near the surface of the solid structure. These layers, known as the main and secondary vortex layers, change with the cyclic flow, and are affecting the shape of velocity profiles within the channel. The appearance of an 'm' shape, a 'slug' shape and a 'parabolic' shape velocity profiles are also depending on the flow amplitude (drive ratio) and flow frequency. The 'parabolic' velocity profile is only found for a certain moment of flow with thick boundary layer. The results indicated that fully developed flow may not be likely for cases presented in this paper. Hence care should be exercised in the use of equations during the analysis of thermoacoustic system. As the parallel-plate structure is usually an important structure of the system, a proper understanding of the dynamics of flow within this structure is crucial. These findings are expected to give better insight for future design of thermoacoustic system.

1. Introduction

Due to the clean working principles that is safer to the environment, thermoacoustics have been recognized as one of the not-in-kind technologies or alternative technologies for refrigeration cycle [1]. Thermoacoustics can also be used for power cycle [2]. In general, thermoacoustic system is a system that is based on thermoacoustic principles where thermodynamic processes for engine and/or refrigerator are obtained via exchange of energy between acoustic wave and solid surfaces of a structure that resembles a porous structure. The thermodynamic process of expansion, compression and heat transfer happen when acoustic wave meets solid surface at a designated condition within the acoustic environment. The basic components of most thermoacoustic systems, as shown in Fig. 1, are the acoustic driver (loudspeaker or alternator), a resonator and a porous structure commonly referred to as a 'stack' or a 'regenerator'. Expansion, compression and heat transfer processes occur due to the changes of pressure and velocity of the flow following the travels of acoustic wave across the structure. The cyclic travel of the working fluid completes the thermodynamic cycle for the system. Many prototypes have been developed across the world including generator [3], refrigerator [4], generator driven by low grade heat [5] and a coupled system of thermoacoustic refrigerator driven by thermoacoustic generator [6]. The simplistic design that uses very minimum moving mechanism reduces

* Corresponding author.
E-mail addresses: fatimah@utem.edu.my (F.A.Z. Mohd Saat), x.mao@leeds.ac.uk (X. Mao).

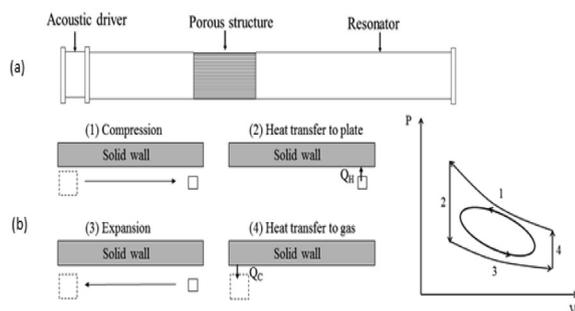Peer review under responsibility of Karabuk University.

Fig. 1. (a) Basic thermoacoustic system (b) Thermodynamic processes within the porous structure inside the system.

maintenance issues and the working principle with the use of noble gas is safe to the environment. The involvement of minimalist components leads to tendency of miniaturizing the device for use in small size applications [7].

Complex fluid flow and energy transfer interaction happens between an oscillatory flow of the acoustic wave and a solid material of the porous structure during the operation of thermoacoustic device. The understanding of the flow behavior and heat transfer in the interior structure in oscillating environments are one of the keys to a better design and development of the system [7,8,9]. Nonlinear behaviors due to the oscillation of flow are among the factors that require attention. Experimental and numerical works suggested that the nonlinearity of flow could lead to unexpected flow that may influence the performance of the system [10,11]. In an attempt to understand the fluid dynamics of flow inside thermoacoustic system, the oscillatory flow across parallel-plate heat exchangers were shown to be best modelled using SST k-ω turbulence models [12]. In the study reported by Ilori et al. [13], the SST k-ω turbulent model was applied for oscillatory flow and heat transfer conditions in three cases with similar tube channels heat exchangers but with three different edge shapes. The results suggested that the presence of edge shapes helps to reduce the complexity in flow that results from the discontinuity of the geometry [13]. The frequency of the thermoacoustic systems is also an important aspect to consider too [14]. For the investigation of the impact of flow frequency, Antao [14] developed an OPTR (Orifice Pulse Tube Refrigeration) that was operated at a constant mean pressure of 1.81 MPa with all other parameters other than frequency set as constant. The system was run at five different values of operating frequency, 55, 60, 62, 65, and 70. The results showed that a lowest gas temperature of 125.75 K was attained after 60 min of operating the OPTR at a frequency of 65 Hz. At that optimum frequency of 65 Hz, the OPTR was not only reaching the lowest temperature but the cool-down time was also the fastest. This was achieved at the highest value of pressure amplitude of the optimum frequency. This shows that flow frequency has impact on thermoacoustic systems.

The design of porous structure used in thermoacoustics (i.e. the 'stack' and the 'regenerator') is also an important aspect to consider. Experimental and theoretical investigations were done by Hariharan et al. [15] to figure out the impact of plate thickness (PT) and plate space (PS) of the stack used in the system. The impact of the length of resonator with constant stack length on the performance of standing wave open end thermoacoustic prime mover was also investigated. The study was conducted to observe the performance of the system in terms of onset temperature difference. The onset temperature was defined as the temperature at which the thermoacoustic effect can be realized. The range of frequency was set at 230 Hz and 250 Hz as the range was reported to be sufficient to drive thermoacoustic refrigerator investigated by

them. The results showed that the PT of 0.3 mm produced a large temperature difference which is useful in generating oscillatory flow compared to the PT of 0.5 mm irrespective of the spacing sizes, PS. On the other hand, by increasing the space between the plates (PS) and the resonator length, the working frequency was observed to decrease for both the plate thickness (PT) of 0.3 mm and 0.5 mm. The onset temperature difference and pressure amplitude also decreased.

Several studies related to the predictions of turbulence oscillatory flow and vortex shedding were also reported [12,16]. It was suggested that turbulence should be considered when designing thermoacoustic devices even for low-amplitude flow conditions. In addition, the effect of the length of the plate, which was not considered in theoretical equation, was also shown to have significant effect on the velocity within the channel of the stacks' structure. The presence of turbulence at low range of flow amplitude and the changes of flow due to dimension of the 'stack' indicated that more investigations are needed to understand the fluid dynamics of flow inside the system and their impact on the system. Experimental approach was also used to investigate the vortex shedding phenomena in thermoacoustic devices [17]. They conducted Particle Image Velocimetry (PIV) measurements of oscillating flow field in and around a thermoacoustic stack. 'Thick and thin plates' were utilized for the stack structure. The results showed that the flows around the ends of the stack were revealed to be quite different. Vorticity layers with positive and negative signs were observed near the solid's surface (boundary layers within the channel) and at the end of the stack (vortex shedding within the open area outside the channel). Similar forms of vortex patterns were also reported by Aben [18]. Aben [18] categorized the vortex patterns into several categories namely the two vortices, four vortices and the vortex street. Two vortices pattern was reported at low Reynolds number followed by the four vortices pattern and the vortex streets as the Reynolds number increases. For "thick-plate", it was reported that concentrated vortices near the edge of the plate was observed [17]. For cases with "thin-plate", the results did not show the formation of well-defined eddies. Instead the presence of elongated layers that extend well outside the channel were observed. The PIV method was also used to investigate the vortex shedding at the ends of the stack and the velocity profile inside the oscillating boundary layers between the plates of the stack [19]. The results indicated that the vortices were not shed further than two acoustic displacement away from the stack edges. The investigation was done for various stack configurations (the plate thickness and spacing and drive ratio). The range of Reynolds numbers were between 200 and 5000. For a more detail understanding about vortex shedding phenomena in the cyclic flow of thermoacoustics, a Particle Image Velocimetry (PIV) was used to record the evolution of vortex shedding within an acoustic cycle, phases-by-phases [20]. For oscillatory flow, the fluid flows in cyclic manner that involves acceleration and deceleration stages of ejection (forward flows) and suction (backward flows) phases. The general trend of vortex showed that it is likely that the flow physics controlling the vortex shedding frequency in the "ejection" stage of the oscillation cycle was similar to that for steady flows [21]. The only difference between oscillatory flow and the steady one-directional flow is that the flow will reverse and then flows forward again repeatedly over time leading to unique disturbances in the flow due to the travel of vortices in and out of structures along the travel distances of flow.

In different investigations, two-dimensional axisymmetric model of a thermoacoustic Stirling engine with a short tube was developed [22]. Three dimensionless parameters namely the Reynolds number (Re), the Keulegan-Carpenter number (KC), and the Womersley number (Wo), were used to describe the flow regime and the vortex characteristics throughout the short tube. The KC

number had been shown to have a direct effect on the transition of streamlines and the development of the vortex. For large cross section where KC < 1, the vortex disappeared in the main flow region and was confined only to location near the short tube. The velocity profile within the tube tends to be flat. The results suggested that increasing the diameter of the short tube is favorable for the purpose of reducing power dissipation. The dimensionless number of Strouhal number was also used in representing the frequency of vortex shedding that appears at the end of the plate [21]. Oscillatory pipe flows were also investigated using three-dimensional direct numerical simulation (DNS) [23]. The study was related to the transition to turbulence in Sexl-Womersley (SW) flows. Sexl-Wormesley flows is the name given to describe oscillatory flow inside pipe. Three Womersley numbers, Wo, of 26, 13, 5 and one constant Reynolds number (Re = 1440) based on the friction velocity and pipe diameter were investigated. The results indicated that the oscillatory flows relaminarized or reached a conditionally or fully turbulence state depending on Wo. The peak of rates decreased with increasing Wo. For high Wo there was no instabilities found near to the wall. For oscillatory flow of thermoacoustics, the channel of the porous structure is usually small and therefore theories derived based on oscillatory flow inside pipe with normal big size diameter may not be appropriately representing the physics of the flow [12]. In oscillatory flow, the vortex shedding and velocity profiles are usually measured as a function of phase angle within an oscillation period and the distance from the stack end into the channel. The time history data of vortex and velocity profiles help in understanding the fluid dynamics that change with time during oscillatory flow cycle. Studies found that the velocity profile at the entry to the channel is never flat, as is the case for piston-induced pipe flows [24,25]. Clearly, several shapes of velocity profile were reported to be seen in the channel within oscillatory flow conditions. However, as stated earlier, flow inside pipe may not be similar to flow across structure (obstructed flow). Unfortunately, the study on fluid dynamics changes within channel due to oscillatory flow across structure are rarely reported. Due to the nature of oscillatory flow that flows forth and back, it is expected that the vortex shedding at the end of plate will give impact on the velocity profile and the boundary layer that were formed within the channel. In oscillatory flow, behavior of flow is also influenced by frequency [23] but the change of behavior of oscillatory flow across structure is again not well understood. In this paper, a focus on the fluid dynamics changes of flow at two values of low range frequencies are reported. Better fluid dynamics understanding of the oscillatory flow within structure of thermoacoustic system will lead to better understanding of gain and losses in the system.

2. Methodology

In this study, investigations of fluid dynamics of oscillatory flow at two different flow frequencies over parallel-plate structure of thermoacoustic system is investigated. The investigations were mainly done using Computational Fluid Dynamics (CFD) models that are validated using data obtained from experiments and theoretical calculations.

2.1. Computational model

The computational domain utilized in this study is based on the experimental setup at Universiti Teknikal Malaysia Melaka [26]. The computational domain, as shown in Fig. 2, covers the areas around the 'stack' structure. A two-dimensional ANSYS CFD model for oscillatory flow across parallel-plates structure inside a standing-wave thermoacoustic environment was solved using
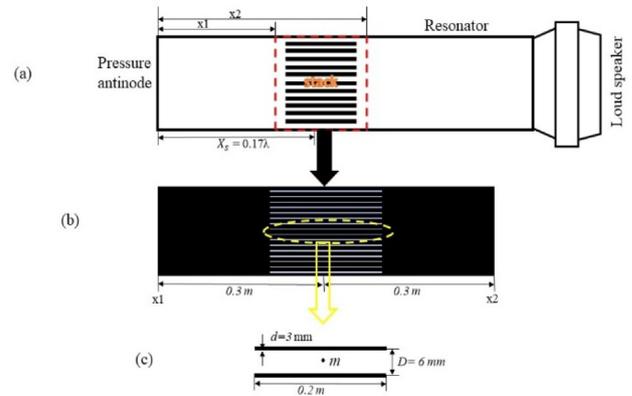

Fig. 2. Quarter wavelength standing-wave experimental setup, (b) the computational domain, (c) the view of a channel between two plates of "stack".

SST k-ω turbulence models. The Shear Stress Transport (SST) model has the advantages of solving flow equations within the boundary layer as well as in the open stream. The introduction of the blending function allows the use of both the k-ω and k-ε turbulence models depending on the distance from the wall. This provides the advantages of models in both the viscous and inviscid flow areas. The combination of the blending function as well as the eddy viscosity model was reported to reveal a very good results of fluid dynamics and heat transfer with closest values to experiment and the model was also shown to be less sensitive to the grid size [27]. This model has also been proven to perform excellently in the case of the presence of adverse pressure gradient as can be found in cyclic flow condition of thermoacoustics [10,12]. Hence the current models are solved using the SST k-ω models. Two different operation frequencies were used: 14.2 Hz and 23.6 Hz. The ideal gas was selected as working fluid at the atmosphere pressure.

The model was created covering a rectangular area of 0.6 m × 0.15 m of the 1/4-wavelength resonator. The stack, which is placed at the middle of the computational domain, is located at 0.18λ from the pressure antinode. The wavelength, λ, is calculated as the speed of sound, c, divided by the frequency of the flow, f. The location of pressure antinode for the quarter wavelength rig is at the rigid end of the resonator. The parallel plates were with length of 200 mm, thickness, d, of 3 mm and spacing, D, 6 mm. The total number of the parallel plates that made the porous structure of the 'stack' are 16 plates. User-defined-function (UDF) codes were used to represent the oscillatory flow behaviors at the inlet and outlet conditions of the model. An oscillatory pressure was assigned as inlet (at x_1 location) boundary condition by using Equation (1). A mass flux was defined as outlet (at x_2 location) boundary condition and the condition is represented using Equation (2).

$$P_1 = P_a\cos(k_a x_1)\cos(2\pi ft) \tag{1}$$

$$m'_2 = \frac{P_a}{c}\sin(k_a x_2)\cos(2\pi ft + \theta) \tag{2}$$

where $P_a, c, k_a, f, t, \theta, x_1 \text{ and } x_2$ are acoustic pressure at the location of pressure antinode, speed of sound, wavenumber, flow frequency (Hz), time, phase and the locations of inlet and outlet of the domain, respectively. The wave number is a function of angular velocity, ω, and it is defined as $k_a = \omega/c$. Two additional boundary conditions were calculated and considered, the turbulent length scale which is defined as $\ell = 0.07D$ and the turbulent intensity is identified as $TI = 0.16(Re)^{-1/8}$. The diameter, D, for the turbulent length scale is based on the height of the resonator. The Reynolds

number for the calculation of turbulent intensity was based on the theoretical velocity amplitude for the location of the related boundary.

Quadrilateral type of mesh was used in this model. Segmentation method of meshing, where computational domain was divided into several parts, was implemented to obtain a better mesh quality for the domain. A denser mesh was applied at locations near the plates to capture the dynamic changes of flow within that area. The meshes used for the simulations were with maximum skewness of 0.053 with maximum aspect ratio of 38.4. A minimum orthogonal of 0.94 was recorded.

The model was solved using transient pressure-based implicit solver with the applications of the Pressure-Implicit with Splitting Operators (PISO) scheme for the pressure–velocity coupling. A least square cells-based method was selected for solving gradient in the numerical models and a second order upwind scheme was selected for the pressure, density, momentum and turbulent kinetic energy equations. Grid independency test was done using three-difference mesh numbers 62920, 106,000 and 133126. Fig. 3 presents the grid independency test result where velocity amplitudes within the area of stack were recorded for models with three different total number of cells.

The cells number of 106,000 was found sufficient to provide solution that is independent of grid size. Although SST model was reported to be less sensitive to the grid size [27], the grid for the current model is ensured to be with $y+$ value that is within the value of unity as a precautional step. This is done to ensure that better boundary layer data can be obtained. The $y+$ value for the selected grid was recorded as 0.98. Transient models were solved with time step size of $1/1200f$ so that convergence could be achieved within 15 to 20 iterations in every time step. The continuity and momentum equations are observed to converged at 10^{-3} while the turbulence equations converged at 10^{-5}. The energy equations converged at 10^{-7}. The unsteady models were solved for a minimum of 7 cycles to reach a steady oscillatory flow condition where data are not anymore changing with cycle. Once this condition is achieved, results are processed for analysis.

2.2. Experimental works

The experimental works were done based on the available quarter wavelength setup of thermoacoustic rig. The rig and the schematic diagram of the experimental setup for both frequencies are as shown in Fig. 4.

The schematic shows the components of standing-wave thermoacoustic device which are the loudspeaker as an acoustic driver, the resonator, and a parallel-plate structure known as 'stack' that is placed at a location of 0.18λ from the hard end of the resonator. An 18-inch subwoofer type loudspeaker (Model 1860 manufactured
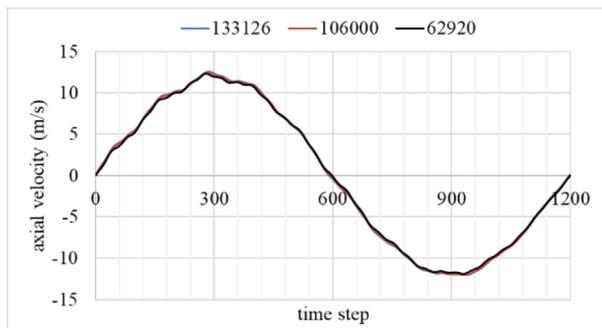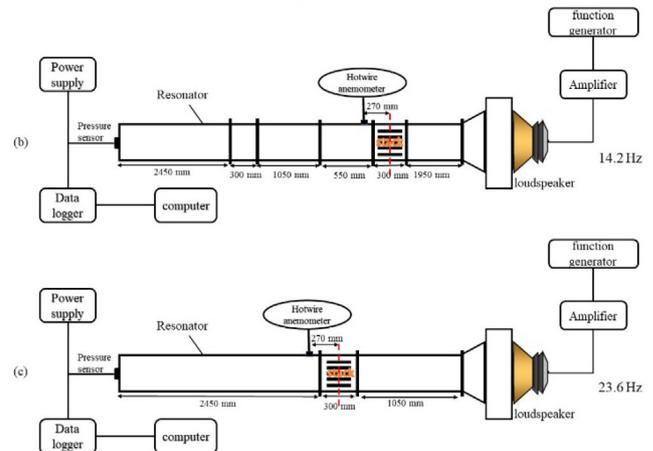

Fig. 4. (a) Real picture of experimental rig, (b) schematic diagram of 14.2 Hz rig, (c) schematic diagram of 23.6 Hz rig.

by Precision Device) was attached to the rig and the output form the speaker is controlled by instruments such as an amplifier (Fletcher FLP MT1201) and a function generator (SG1005-DDS). A dynamic pressure sensor (Endevco model 8510B) was used to measure pressure at the location of pressure antinode. The pressure sensor is connected to data logger and a direct-current (DC) power supply was used to control the input voltage so that it does not exceeds the limit allowed for the sensor. Data from the data logger was processed using Windaq software. A hot wire (SENTRY model ST732) was used to measure the amplitude of velocity for the flow. RI-APPLICATION SOFTWARE was utilized to read the values of the velocity.

The experimental data was collected only for the purpose of model validation. For this reason, the hot wire sensor was placed at a location of 270 mm from the middle point of the stack (a location shown in Fig. 4. (b) and (c)) to read the velocity amplitude at that point. The hotwire anemometer is a stand-alone sensor with built-in signal conditioning system. The value of velocity was taken straight away from the screen of the instrument.

3. Validation of model

The model was validated using data at location 270 mm away from the end of plate. The validation was done by comparing the results of velocity amplitude from the model to the measured values obtained from experimental works. Comparison to theoretical values was also done. The results are as shown in Fig. 5.

It is noteworthy that the models were solved for thermoacoustic flow conditions based on the available test rig. Hence, the theoretical solution based on the Rott's Linear Thermoacoustic Theory is used for the purpose of verification [8]. The theoretical equation that was used to calculate the velocity amplitude is as shown in Equation (3):
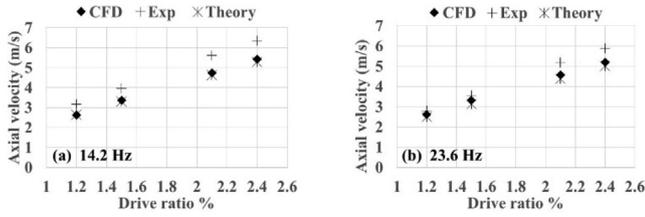

Fig. 3. Grid independency test at three different mesh numbers of 133126, 106,000 and 629,620.

Fig. 5. Validation of the model with theoretical data at point 'm' for cases with frequency of (a) 14.2 Hz and (b) 23.6 Hz.

$$u = \frac{k_a P_a}{\Phi \omega \rho} \sin(k_a x) \qquad (3)$$

The terms Φ, ω, and ρ are the porosity of the domain, the angular velocity and the density of the fluid. location of $\times$ is the location where data for validation was taken. For the purpose of validation, the location of data collection was chosen with an intention of minimizing potential errors due to disturbances of flow that occur near the parallel-plate structure. The porosity (which is defined as the ratio of the volume of the gas within the stack to the total volume of the stack) at this location where axial velocity amplitude was measured experimentally is 100%. Due to the limitation of the available experimental setup, reliable data could not be collected at drive ratio lower than 1%. The drive ratio is defined as the ratio between the maximum amplitude of oscillating pressure at the location of pressure antinode and the mean pressure of the flow. As drive ratio increases the velocity amplitude increases. When the drive ratio increases higher than 2.6%, there was noticeable vibration that could interfere with the data. Hence the experimental works were limited to drive ratio between 1% and 2.6%. Theoretical calculations were used to verify CFD results when experimental data are unavailable. Fig. 5 (a) and (b) show the validation of the model by using plot of axial velocity amplitude at several drive ratios for both flow frequencies.

In general, the results from the CFD models are within the values gained from theory and experiments. Experimental values are slightly higher than the values predicted by the CFD and theoretical formulas. The differences are more noticeable at lower frequency of 14.2 Hz. The differences between CFD and experiment is also more consistent for all the drive ratios at this low frequency. At higher frequency of 23.6 Hz, the differences between CFD and experiment is only noticeable at higher drive ratio. The reason for the differences is unclear but it could be related to the disturbances in the flow inside the experimental rig. One might expect a greater difference between CFD and theory for high flow frequency because high flow frequency involves rapid flow that could introduce bigger nonlinearity to the flow. But for this experimental works, in order to keep the flow at resonance the low frequency flow involves longer rig than the high frequency flow. There may be a possibility that additional streaming is bigger in the long resonator and this streaming is affecting the values of the axial velocity amplitude. However, for the purpose of model's validation, the experimental data is found sufficient to be used since the trend and values from CFD models are within the range of theoretical predictions and experimental works.

The changes of axial velocity amplitude with time over one flow cycle is as shown in Fig. 6. The velocity amplitude was plotted for 20 phases of one flow cycle at location "m" for all cases of drive ratio from 0.3% up to 3%. The location 'm' is as defined earlier in Fig. 2.

CFD data was compared with theory. For theoretical calculation, the porosity of the domain at this location is calculated to be 68%. A relatively good match was seen between the results from CFD and theory. The fluid accelerates in positive value during the first
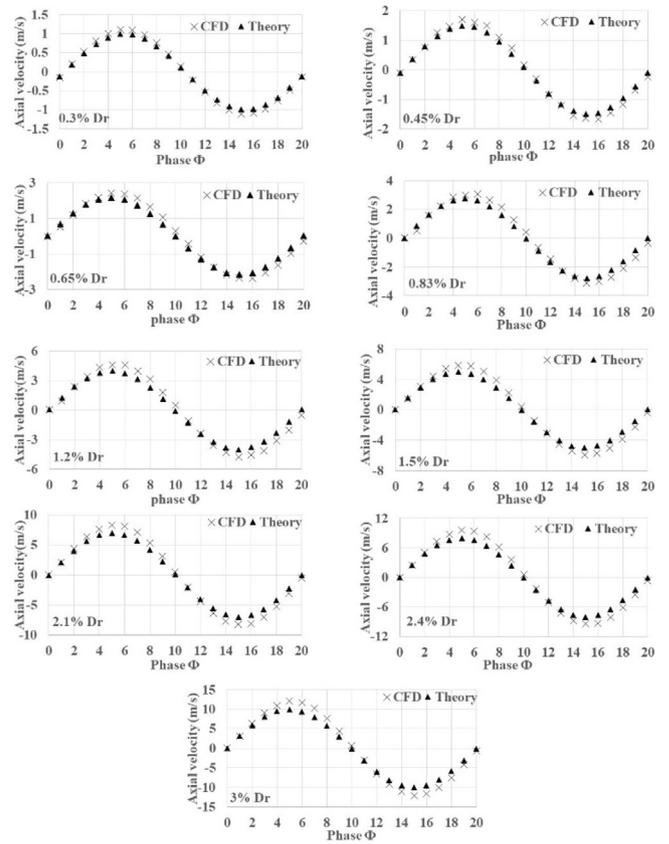

Fig. 6. Validation the model with theoretical data at point "m" for all cases of drive ratio with frequency of 14.2 Hz.

quarter of the cycle (phases 0 to 5) and then decelerates (phases 6 to 10) before the flow changes direction with negative amplitude of velocity. In the negative part of the amplitude (the second half of the cycle), the flow accelerates between phases 10 to 15 and then decelerates between phases 16 to 20. After that the flow cycle repeats. Differences in velocity amplitude can be seen especially during the deceleration stages where flow starts slowing down before it changes its direction. This could be due to the flow nonlinearity affects that can be captured by the two-dimensional SST k-ω turbulence model. In the theoretical formula, as presented in Equation (3), the solution is for the assumption of linear one-dimensional flow. Hence, the difference of amplitude between theory and experiment that happens between phases 4 to 20 may be due to the travels of vortex in and out of the channel as the flow oscillates back and forth across the structure. This point is to be elaborated further in later section.

4. Boundary layers and velocity profiles within the channel

Oscillation of flow leads towards flow that oscillates back and forth across structures. In this case, the oscillatory flow within the channels of the 'stack' in the investigated thermoacoustic environment is as shown in Figs. 7, 8 and 9.

Fig. 7 shows the comparison of results at two different flow frequencies. The results are for the boundary layer and the velocity profiles within the channel for flow frequencies of 14.2 Hz and 23.6 Hz with 0.83% drive ratio. Three phases were selected which are Φ1, Φ5 and Φ8. These three phases represent the acceleration and deceleration stages of positive flow amplitude. During this first half of the flow cycle, the fluid flows from left to right. At Φ8, the fluid is still flowing forward but in deceleration amplitude. It is
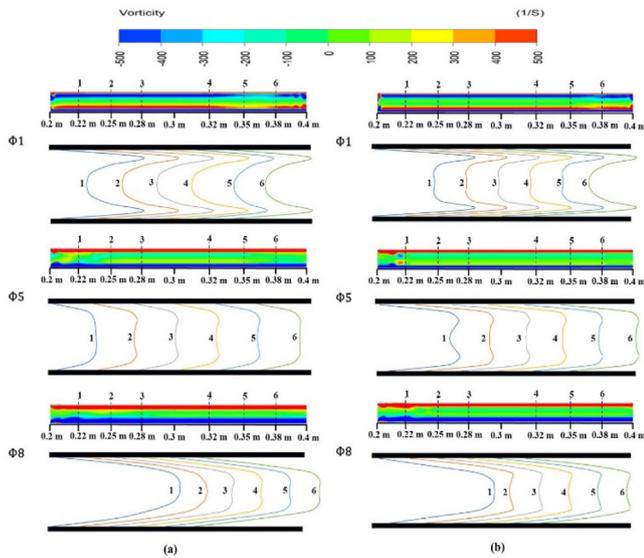
Fig. 7. Boundary layers and velocity profiles within the channel for flow with 0.83% drive ratio and flow frequency of (a) 14.2 Hz and, (b) 23.6 Hz.

Fig. 9. Boundary layers and velocity profiles within the channel for flow with 3% drive ratio and flow frequency of (a) 14.2 Hz and, (b) 23.6 Hz.

Fig. 8. Boundary layers and velocity profiles within the channel for flow with 1.5% drive ratio and flow frequency of (a) 14.2 Hz and, (b) 23.6 Hz.
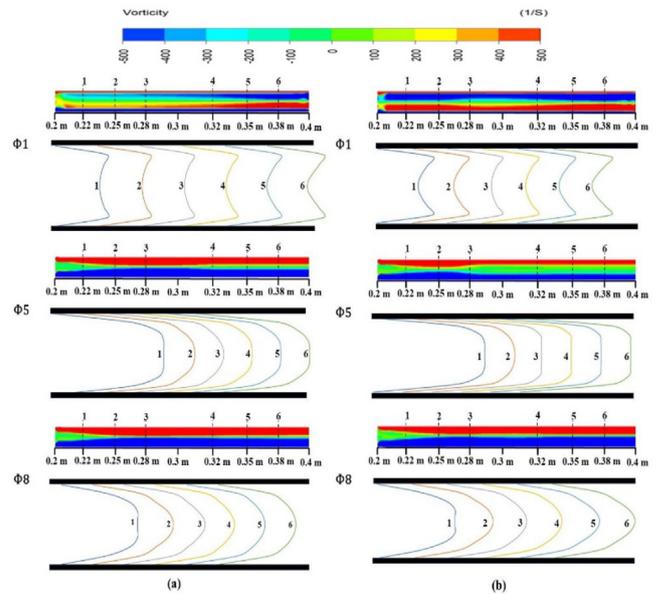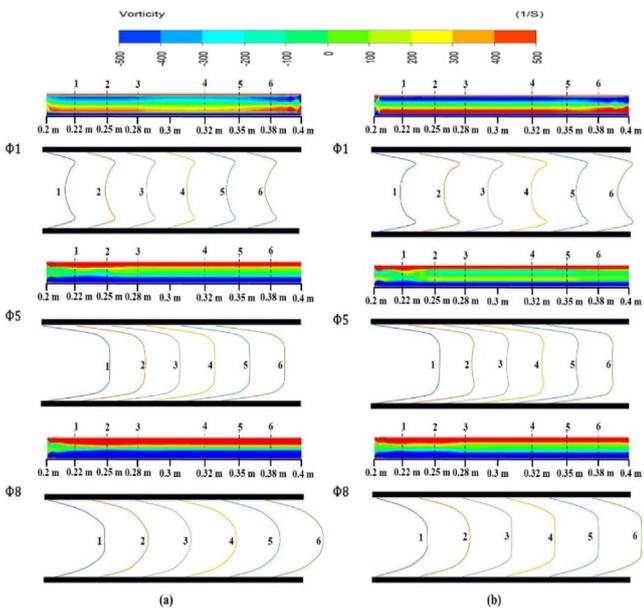
observed that the changes in boundary layer and velocity profiles in the second half of the cycle (with negative values of velocity) are similar to the first half of the cycle (with positive values of velocity). Velocity profiles were plotted for six locations within the channel. Two layers of boundary layer were detected for both frequencies. The main layer is located exactly next to the surface of the plate. The secondary layer which is located next to the main layer was also noticed in the flow and this layer is with opposite sign of the main vortex layer. The appearance of the secondary layer can be seen as a very thick layer at phase Φ1. This is representing the strong effect of the change of flow direction that is about to take place at this phase. The change of flow creates rotationality of flow near the boundary layer as the mean flow is changing its direction. The appearance of the secondary layer seems stronger for high frequency of 23.6 Hz compared to the

low frequency. For the cases shown in Fig. 7, the amplitude of flow is controlled to be at the same amplitude (0.83% drive ratio). At higher frequency, the fluid flow rapidly in terms of time if compared to low flow frequency. The strong appearance of the secondary layer is expected to be due to the rapidness of flow at the higher value of frequency. As velocity increases to Φ5, the secondary layer faded but there was a pair of secondary vortices that can be seen travelling within the channel especially at high frequency of 23.6 Hz. This represents the travels of high amplitude of flow at this Φ5 (refer to Fig. 6 as guidance of flow amplitude). The high amplitude of main flow tends to create bigger rotationality of flow that is seen in the result as the travel of a pair of vortices at the left end of the channel. As the flow decelerates to Φ8, the secondary layer seems disappearing from the flow. This is consistent with the fact that the rotationality of flow near the boundary layer becomes weaker as the amplitude of flow becomes smaller. It is also observed that the main boundary layer for low frequency is slightly thicker than that for high frequency. This is in tandem with theoretical relationship between viscous boundary layer and the flow frequency [8].

It can also be observed that the appearance of boundary layers is somehow affecting the velocity profiles within the channel of the plates. Three shapes of axial velocity profiles were noted for both frequencies. The 'm' shape of velocity profile appeared at low amplitude in phase Φ1. This 'm' shape profile seems to appear as a result of the strong appearance of both the main and secondary layer of boundary layer. The opposite signs of vorticity values for the main and the secondary layers mean that the direction of flow within the layers is different. This is the feature of flow at Φ1 as the fluid is starting to flow in forward direction. As a result, an 'm' shape velocity profile is seen at this phase.

A 'slug' shape of velocity profile can be seen at the maximum amplitude of flow that happens in phase Φ5. This profile is represented by almost a flat profile at the center of the channel. A weak appearance of secondary boundary layer leads to this kind of velocity pattern. At this phase, a more uniform velocity value can be obtained at the center of the channel. The 'm' shape profile at location '1' of the high flow frequency of 23.6 Hz happened due to the presence of a pair of vortices that travels within the channel.

For phase Φ8, in deceleration stage, a 'parabolic' shape of velocity profiles is detected at several locations. This 'parabolic' type of velocity profile appeared at locations with thick boundary layer. Differences in the pattern of velocity profiles for both flow frequencies can be seen. A 'parabolic' velocity profile shape can be seen at locations '1′' and '2′' for low frequency at phase Φ8 and a somewhat 'slug' like profile with small 'dent' at the center for the other locations. For high frequency, the boundary layer at location '1′' is a bit thicker and therefore the velocity profile appeared as a 'parabolic' shape. At other locations, the velocity profiles resemble an 'm' shape profile.

Fig. 8 (a) and (b) show the boundary layer and velocity profiles within the channel for a slightly higher drive ratio of 1.5% for both the investigated flow frequencies. By comparing the results of Fig. 7 and Fig. 8, it can be seen that the boundary layer becomes thicker as the drive ratio increases. In addition, the secondary layer appeared stronger than that for 0.83% drive ratio. At high drive ratio, the flow amplitude is bigger. As a result, the impact of the main flow on the velocity profile, particularly at the center of the channel, is greater compared to that of the low drive ratio. At 1.5% drive ratio, the 'm' shape profile is only seen at Φ1. As the flow amplitude is highest at Φ5, a 'slug' like profile is observed throughout the channels for all the six locations. At phase Φ8, in deceleration stage, both the 'slug' and 'parabolic' shapes of velocity profiles were formed depending on location. Generally, the velocity profiles for the six locations of the low flow frequency seems more consistent compared to that for high frequency. The consistent trend of velocity profile throughout the channels indicates the presence of fully developed flow condition within the channel.

Fig. 9 (a) and (b) show the boundary layer and velocity profiles within the channel at higher drive ratio of 3%. For low amplitude flow during phase Φ1, the velocity profiles appeared as 'm' shape for both frequencies. The appearance of secondary layer is stronger at this high drive ratio.

At the maximum velocity amplitude of phase Φ5, a combined shape of 'slug' like and 'parabolic' like profiles is seen for both flow frequencies. At low flow frequency, the 'parabolic' like profile is more dominant while at high frequency the 'slug like profile' is more dominant. The 'parabolic' profile of low frequency at Φ5 is consistent with the consistency of thick boundary layer throughout the channel. Thin layer is only seen at location '1′' of the low 14.2 Hz frequency leading to the 'slug' like profile there. At higher frequency of 23.6 Hz, a significantly thicker layer is seen at the first three locations of '1′' to '3′' and then afterwards the layer is thinner. As a result, all the profiles at this high flow frequency forms a 'slug' like profile except for location '2′' where the boundary layer is thicker. The thick layer at that location represents the travel of flow during that stage. At the deceleration stage of phase Φ8 all the locations appeared with somewhat a 'parabolic' like shape except for location '1′' where the profile resembles a 'slug' shape for both frequencies. Again, the thickness of the layer is consistent with the presence of either 'slug' profile or 'parabolic' profile.

The changes of velocity profiles and the boundary layers influence the dissipation of flow and hence will give impact on the performance of thermoacoustic system. This behavior of thermoacoustic flow condition indicates that the flow may not be simply treated as fully developed and hence the impact of this on the fluid dynamics and heat transfer analysis of the energy system may need to be considered.

5. Vortex shedding at the end of the plates.

The boundary layers that feature two layers with opposite signs and their impact on velocity profiles indicate the importance of understanding the vortex shedding that forms at the end of the
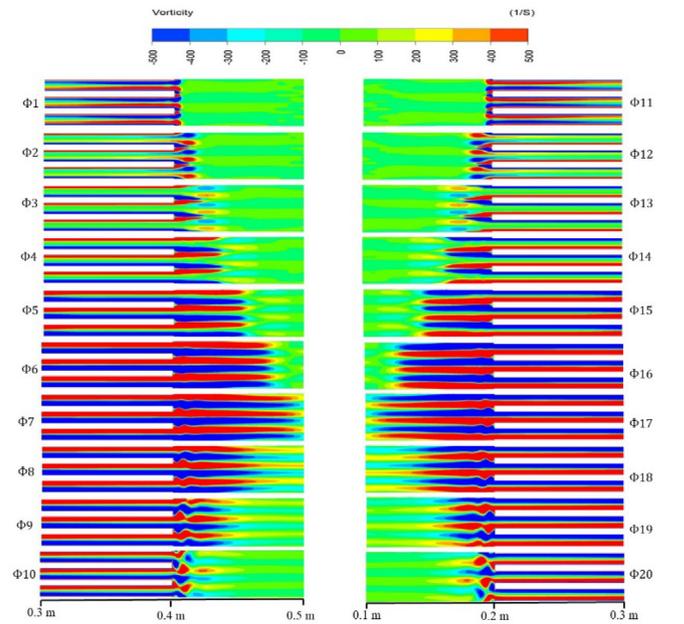

Fig. 10. Vorticity contour for oscillatory flow at 3% drive ratio and a frequency of 14.2 Hz.

plates. Fig. 10 shows the development of vortex shedding at the end of plates over twenty phases of a flow cycle.

The results are shown for the maximum drive ratio of 3% with low flow frequency of 14.2 Hz. The first ten phases (Φ1 to Φ10) represent positive values of velocity where fluid flows forward. Then the fluid reveres during the second half of the cycle as presented by phases Φ11 to Φ20. During the first quarter of the flow cycle (Φ1- Φ5), fluid accelerates in forward direction. Phase Φ5 presents the peak of velocity amplitude when the fluid flows in forward direction. Later, in phases (Φ6- Φ10), the fluid is still flowing forward but it is slowing down (deceleration). The same happens when the fluid reverses (i.e. fluid accelerates at Φ11- Φ15 and then decelerates at Φ16- Φ20).

At low amplitude of phases Φ1 and Φ11, the secondary viscous layer at the middle of the channel appeared thinner than the parts towards the end of the plates. Secondary viscous layer at the first phase was thicker than the main viscous layer. At the end of the plates, both the viscous layers flow out towards the open area while still attaching to the plates. At phases Φ2 and Φ12 the secondary vortex pulls out from the channel and travels to a larger distance towards the open area compared to the travel of the main layer. The main layer is still attaching to the plates. Circular shape of secondary vortex starts forming at these phases. At phase Φ3 and Φ13 the secondary layer at the end of plates becomes weaker and still with circular shape. Then the secondary layer becomes weaker while travelling further towards the open area as the fluid continues to flow forward up to phase Φ10. In the meantime, the main boundary layer extends out forming an extended vortex structure that is attached to the plates. The maximum distance of the extension is seen at the deceleration stage of phase Φ7. This indicates that the attached vortex is still expanding out even when the fluid velocity reduces during the deceleration stage. The same pattern is seen when the flow reversed. The attached main vortex then becomes thinner and takes a sharp shape at phases Φ8 up to Φ10 and a similar structure is seen when fluid flows in opposite direction. Interestingly, the vortex shedding patterns between forward flow (Φ1- Φ10) and reversed flow (Φ11-Φ20) are symmetrical when comparison is made between phases with similar amplitude of flow. At the last three phases of Φ8, Φ9 and Φ10, there is a wiggle

pattern of vortex shedding for both flow directions. At the last phases of Φ10 and Φ20 the pattern of vortex shedding at the end of the plates was broken, this is probably occurring due to the flow which is about to change direction (reversing). In general, the vortex shedding is always attached to the plates. The breaks of vortex which at some condition may looks like a vortex street is actually the feature of the reversing flow in this type of flow. Symmetrical pattern of vortex was observed between the phases when the fluid flows forward and when the flow reversed.

Table 1 presents the displacement of flow in each drive ratios for both the investigated flow frequencies. The displacement, δ, was calculated using theoretical equation of $v = \omega\delta$, where the maximum velocity amplitude, v, was used and the value was taken from phase Φ5 of the flow cycle. The angular velocity, ω, is calculated as $\omega = 2\pi f$ using the flow frequency, f. These values of displacement, as tabulated in Table 1, are used to help illustrating the impact of flow frequency on the travel distance of vortex at the end of the plate and into and out of the plate's channel. As expected, the displacement is bigger as the drive ratio increases. This indicates that the vortex has tendency to be displaced to larger distance as drive ratio increases. For low frequency the vortex shedding is displaced or elongated to almost double the distance of the high frequency of 23.6 Hz.

Fig. 11 illustrates the extension of the vortex shedding at the end of plates for both the frequencies of 14.2 Hz and 23.6 Hz. Results are shown for three different drive ratios which are 0.83%, 1.5% and 3%. The vorticity contour is shown for an area covering the middle of the plates up to 200 mm to the open area on the right side of the plates. In the area within the channel of the plates, the boundary layer for low frequency is thicker than that for high frequency.

Consistent with the results shown earlier, there is a secondary viscous layer that appeared clearly at low amplitude for both frequencies. This secondary viscous layer can be seen next to the main layer with different signs (blue color that represents negative vortex and red color that represents positive vortex). There is an area where thin secondary layer is detected, and this appeared clearly within the channel at phase Φ1 for low frequency of 14.2 Hz. The thin area is almost not seen for high frequency of 23.6 Hz probably due to the common feature of the thin viscous penetration depth of the high flow frequency. As drive ratio increases the secondary vortex becomes thicker and stronger for both frequencies. The secondary viscous layer flows out of the stack and this can be clearly seen at the maximum amplitude of flow in phase Φ5. For all the drive ratios, the pair of circular vortex shedding that comes from the secondary viscous layer appeared stronger at higher frequency. Vortex shedding at the end of the stack for both frequencies are found always attached to the plates. Consistent with the theoretical displacement data from Table 1, the vortex shedding at the end of the plates for low frequency of 14.2 Hz was found to elongate to longer distance than that for high frequency of 23.6 Hz.
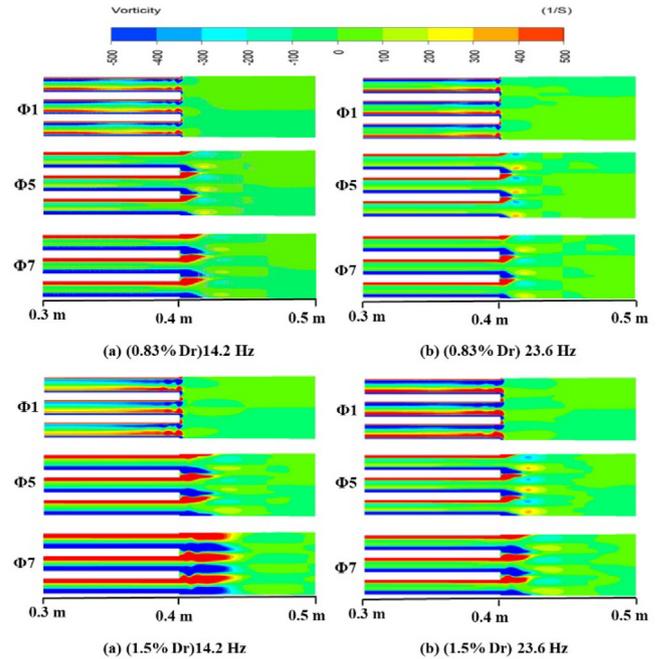

Fig. 11. Vortex structure within and at the end of the plate for three different drive ratios for both frequencies.

Table 2 shows the results coming from the observation of the secondary vortex pattern for all the drive ratios that was computationally solved for both the investigated frequencies of 14.2 Hz and 23.6 Hz. The results are shown for the first half of the cycle when fluid flows forward from left to right. At low frequency of 14.2 Hz, the secondary vortex is seen for all cases except for the lowest drive ratio of 0.3%. In general, the secondary vortex of low flow frequency disappeared from the open area at earlier phases compared to that of the high flow frequency. It is also observed that the secondary vortex is not seen in the open area during most of the deceleration stage of the flow.

Clearly, the secondary vortex and the secondary boundary layers are the feature of the main stream of the flow that oscillates across the structure of thermoacoustic system. The main boundary layer next to the plate is the viscous layer that developed due to the no slip condition at the wall. The presence of both the main and secondary layers lead to three different shapes of velocity profiles that appear within the channel in cyclic manner. These changes of velocity profiles and the special feature of the main and secondary vortices may give impact on the time-history development of thermoacoustic effects within a thermoacoustic system.

Table 1
Extension of vortex travels at the end of the stack for both frequencies.

Drive ratio%	14.2 HzDisplacement (mm)	23.6 HzDisplacement (mm)
0.3	12.32	6.94
0.45	18.94	10.72
0.65	24.43	15.71
0.83	33.73	20.50
1.2	51.44	29.60
1.5	65.79	37.02
2.1	92.91	52.26
2.4	106.81	59.95
3.0	135.39	75.12

Table 2
The observation of the secondary vortex layer for both frequencies.

Drive ratio%	14.2 Hz		23.6 Hz	
	Start (phase Φ)	Disappear (phase Φ)	Start (phase Φ)	Disappear (phase Φ)
0.3	–	–	Φ1	Φ2 - Φ10
0.45	Φ1	Φ3 - Φ10	Φ1	Φ4 - Φ10
0.65	Φ1	Φ4 - Φ10	Φ1	Φ5 - Φ10
0.83	Φ1	Φ5 - Φ10	Φ1	Φ6 - Φ10
1.2	Φ1	Φ5 - Φ10	Φ1	Φ6 - Φ10
1.5	Φ1	Φ4 - Φ10	Φ1	Φ6 - Φ10
2.1	Φ1	Φ4 - Φ10	Φ1	Φ6 - Φ10
2.4	Φ1	Φ4 - Φ10	Φ1	Φ6 - Φ10
3.0	Φ1	Φ4 - Φ10	Φ1	Φ6 - Φ10

6. Conclusion

This paper presents the investigation of velocity profiles and vortex changes across a porous structure known as 'stack' for thermoacoustic system. Vortex shedding at the end of parallel-plates was also discussed. Two-dimensional ANSYS FLUENT CFD turbulence models for flow frequencies of 14.2 Hz and 23.6 Hz were validated using experimental data and theoretical formula. There are three shapes of velocity profiles that formed within the channel as the fluid oscillates across the stack. The profiles are labelled as 'm' shape, 'slug' shape and 'parabolic' shape. These shapes occurred at different phases of the flow depending on the drive ratio and the velocity amplitude within the drive ratio itself. The thickness of the boundary layers that forms at both surfaces of the channel (top and bottom) have significant effect on the velocity profiles. The 'parabolic' shape of velocity profile can be found happening when the boundary layers are thick. The results indicated that there are two vortex layers observed for both investigated flow frequencies. The first layer is the main layer adjacent to the surface of the plate while the second layer is the one developed between the main layer and the center of the channel. The secondary vortex layer for high frequency of 23.6 Hz was stronger than that for low frequency. This secondary vortex structure represents the fluctuation of flow which leads to the m-shape velocity profiles within the channel. The distance of vortex travels at the end of plate changes with the change of flow amplitude as flow oscillates back and forth across the structure. At low frequency, the fluid flows to a larger distance but at a slower pace. As frequency increases, the fluid oscillates in a more rapid manner. It was observed that the vortex shedding at the end of the plates for low flow frequency of 14.2 Hz was elongated to larger distance compared to that at high frequency. The main vortex layer that sheds at the end of the stack is found as always attached to the plates for both frequencies. The current study focusses on the fluid dynamics of the flow only. The special feature of main and secondary vortex as well as the time history changes of velocity profiles in this cyclic flow are expected to be affected by the presence of temperature field of thermoacoustic environment. Hence, study in this direction is needed in the future to help better understanding on the impact of fluid dynamics and heat transfer on the design of future thermoacoustic systems.

CRediT authorship contribution statement

Waleed Almukhtar Allafi: Writing - original draft, Investigation, Validation, Data curation. **Fatimah Al Zahrah Mohd Saat:** Conceptualization, Formal analysis, Project administration, Supervision, Writing - review & editing. **Xiaoan Mao:** Writing - review & editing.

Declaration of Competing Interest

The authors declare that they have no known competing financial interests or personal relationships that could have appeared to influence the work reported in this paper.

Acknowledgments

References

[1] S. Choi, U. Han, H. Cho, H. Lee, Review: Recent advances in household refrigerator cycle technologies, Appl. Therm. Eng. 132 (2018) 560–574.

[2] K.O.A. Abdoulla-Latiwish, X. Mao, A.J. Jaworski, Thermoacoustic micro-electricity generator for rural dwellings in developing countries by waste heat from cooking activities, Energy 134 (2017) 1107–1120.

[3] Z. Wu, L. Zhang, W. Dai, E. Luo, Investigation on a 1 kW traveling-wave thermoacoustic electrical generator, Appl. Energy 124 (2014) 140–147.

[4] G. Yu, E. Luo, W. Dai, Advances in a 300 Hz thermoacoustic cooler system working within liquid nitrogen temperature range, Cryogenics 50 (2010) 472–475.

[5] X. Zhang, J. Chang, S. Cai, J. Hu, A multistage travelling wave thermoacoustic engine driven refrigerator and operation features for utilizing low grade energy, Energy Convers. Manage. 114 (2016) 224–233.

[6] E.M. Sharify, S. Hasegawa, Traveling-wave thermoacoustic refrigerator driven by a multistage traveling-wave thermoacoustic engine, Appl. Therm. Eng. 113 (2017) 791–795.

[7] H. Agarwal, V.R. Unni, K.T. Akhil, N.T. Ravi, R.I. Sujith, B. Pesala, Compact standing wave thermoacoustic generator for power conversion applications, Appl. Acoust. 110 (2016) (2016) 110–118.

[8] Swift G. W., 2002. Thermoacoustics: A Unifying Perspective for Some Engines and Refrigerators. New York: Acoustical Society of America, ch. 4.

[9] A.A. Rahman, X. Zhang, Prediction of oscillatory heat transfer coefficient for a thermoacoustic heat exchanger through artificial neural network technique, Int. J. Heat Mass Transf. 124 (2018) 1088–1096.

[10] F.A.Z. Mohd Saat, A.J. Jaworski, The effect of temperature field on low amplitude oscillatory flow within a parallel-plate heat exchanger in a standing wave thermoacoustic system, Applied Sciences 7 (2017) 417, https://doi.org/10.3390/app7040417.

[11] K. Kuzuu, S. Hasegawa, Effect of non-linear flow behavior on heat transfer in a thermoacoustic engine core, International Journal of Heat and Mass Tranfer 108 (2017) 1591–1601.

[12] F.A.Z. Mohd Saat, A.J. Jaworski, Numerical predictions of early stage turbulence in oscillatory flow across parallel-plate heat exchangers of a thermoacoustic system, Applied Sciences 7 (2017) 673, https://doi.org/10.3390/app7070673.

[13] Ilori O.M., Mao, X., Jaworski, A. J, 2015. Numerical simulation of oscillatory flow and heat transfer in the heat exchangers of thermoacoustic systems. In Proceedings of ICR2015. International Institute of Refrigeration.

[14] Antao, D. S. PhD Dissertation. Effects of Acoustic and Fluid Dynamic Interactions in Resonators: Applications in Thermoacoustic Refrigeration. Drexel University, 2013.

[15] N.M. Hariharan, P. Sivashanmugam, S. Kasthurirengan, Influence of stack geometry and resonator length on the performance of thermoacoustic engine, Appl. Acoust. 73 (10) (2012) 1052–1058.

[16] F.A.Z. Mohd Saat, E. Mattokit, S.H.A. Mustaffa, N.M. Ghazali, Numerical study of turbulence related to vortex shedding structures of an oscillatory flow in thermoacoustic energy system, Energy Procedia 156 (2019) 239–243, https://doi.org/10.1016/j.egypro.2018.11.135.

[17] P. Blanc-Benon, E. Besnoin, O. Knio, Experimental and computational visualization of the flow field in a thermoacoustic stack, Comptes Rendus - Mecanique 331 (1) (2003) 17–24, https://doi.org/10.1016/S1631-0721(02)00002-5.

[18] C.H. Aben, P.R. Bloemen, J.C.H. Zeegers, 2-D PIV measurement of oscillatory flow around parallel plates, Experimental Fluids 46 (2009) 631–641.

[19] A. Berson, M. Michard, P. Blanc-Benon, Measurement of acoustic velocity in the stack of a thermoacoustic refrigerator using particle image velocimetry, Heat Mass Transf. 44 (8) (2008) 1015–1023, https://doi.org/10.1007/s00231-007-0316-x.

[20] L. Shi, Z. Yu, A.J. Jaworski, Vortex shedding flow patterns and their transitions in oscillatory flows past parallel-plate thermoacoustic stacks, Exp. Therm Fluid Sci. 34 (7) (2010) 954–965.

[21] L. Shi, Z. Yu, A.J. Jaworski, Investigation into the Strouhal numbers associated with vortex shedding from parallel-plate thermoacoustic stacks in oscillatory flow conditions, European Journal of Mechanics B/Fluids 30 (2011) 206–217.

[22] P. Yang, H. Chen, Y. Liu, Numerical investigation on nonlinear effect and vortex formation of oscillatory flow throughout a short tube in a thermoacoustic Stirling engine, J. Appl. Phys. 121 (21) (2017).

[23] D. Feldmann, C. Wagner, Direct numerical simulation of fully developed turbulent and oscillatory pipe flows at, J. Turbul. 13 (2012) N32.

[24] J.H. Gerrard, M.D. Hughes, The flow due to an oscillating piston in a cylinder tube: a comparison between experiment and a simple entrance flow theory, J. Fluid Mech. 50 (1971) 97–106.

[25] G. Yamanaka, H. Kikura, Y. Takeda, M. Artomi, Flow measurement on an oscillating pipe flow near the entrance using the UVP method, Exp. Fluids 32 (2002) 212–220.

[26] F.A.Z. Mohd Saat, D. Johari, E. Mattokit, DeltaE modelling and experimental study of a standing wave thermoacoustic test rig, Journal of Advanced Research in Fluid Mechanics and Thermal Sciences 60 (2) (2019) 155–165.

[27] Menter F., Carregal Ferreira J., Esch T., Konno B 2003. The SST turbulence model with improved wall treatment for heat transfer predictions in gas turbines. In Proceedings of the International Gas Turbine Congress, Tokyo, November 2-7 2003.